# Pressure Infiltration of Aluminum Melts into a Loose Bed of Hollow Cenosphere Particles

JEONGKYUN KIM,[1,2] AMIR KORDIJAZI ⦿,[1,3,4] and PRADEEP ROHATGI[1]

1.—Materials Engineering Department, University of Wisconsin-Milwaukee, 3200 N. Cramer St., Milwaukee, WI 53211, USA. 2.—Materials Science and Engineering Department, Adama Science and Technology University, P.O. Box 1888, Adama, Ethiopia. 3.—Colleges of Nanoscale Science and Engineering, SUNY Polytechnic Institute, Albany, NY 12203, USA. 4.—e-mail: kordija2@uwm.edu

Experiments on pressure infiltration of pure aluminum melts in loose beds of hollow spherical particles were conducted. An analytical analysis on the melt infiltration in a bed of hollow spherical particles was performed. The solidified layer volume fraction on the particles and their apparent volume fraction were analyzed with respect to the ratio of particle wall thickness and particle radius ($t/R$). The effect of the apparent volume fraction on the threshold pressure, pressure drop, infiltration length, melt temperature, melt flow, and melt viscosity was analyzed. The analysis showed that a higher particle temperature and a lower ratio of $t/R$ decrease the apparent volume fraction of the solidified layers, which results in a lower threshold pressure, longer infiltration length, higher melt temperature around the particles, and higher melt velocity. These results were used to explain the infiltration of the melt into a bed of hollow particles and suggest the benefit of hollow particles for synthesizing composites using melt infiltration techniques.

## INTRODUCTION

Metal matrix particulate composites (MMCs) frequently contain ceramic particulates dispersed in the matrix. The ceramic particles present in the matrix act as reinforcements and impart unique properties, such as improved tribological and mechanical properties.[1] Out of the many techniques to synthesize MMCs, stir casting technique has been widely adopted because of its simplicity and low cost. This technique includes the addition of reinforcements into the melt using a mechanical impeller, followed by pouring of the melt containing suspended particles into the mold. This technique can lead to a non-uniform distribution of the particles in the melt due to the tendency of floatation or settling of particles in the melt,[2,3] resulting from differences in the density between the particles and the melt.[4]

In addition, during solidification, the interactions between the moving solid/liquid interfaces and the reinforcements lead to a non-uniform distribution of reinforcements in the microstructure on a microscopic scale in the interdendritic regions due to the pushing of particles by the solid/liquid interfaces.[5] Addition of increasing volume percentages of particles into the melt progressively increases the viscosity of the melt. Therefore, the volume percentage of particles which can be added into the melt is limited to keep the viscosity of the liquid below the acceptable limits required to make quality shaped castings. The maximum volume fraction of SiC particles which can be added into aluminum alloys by stir mixing is found to be around 25–30 vol%,[6] due to increases in the viscosity of the melt. The microstructures of composites synthesized using the stir mixing technique provide segregation of the particles in the interdendritic region due to the velocity of solid/liquid interfaces, which is lower than the critical interface velocity, above which the particles are captured by the interfaces.[7–9]

On the contrary, the pressure infiltration technique can produce MMCs containing much higher volume fractions of reinforcements in the matrix;

pressure infiltration also leads to a much more uniform distribution of particles in the casting since the particles are not free to move larger distances within the melt.[10] The previous literature has shown the viability of the pressure infiltration of Al/SiC MMCs. The effects of various parameters such as process temperature,[11] wettability of ceramic reinforcements by liquid aluminum,[12] and interfacial interactions[13] in addition to the properties of the final product including thermal conductivity,[14] thermal expansion coefficient (CTE),[15] wear,[16] and corrosion resistance,[17] have been investigated. However, when the ceramic particles and metallic melts are not wettable, the pressure infiltration technique requires a higher external force to infiltrate the melt into the bed of long or short fibers, or the particles to overcome the capillary resistance. Once the applied pressure is higher than the critical threshold pressure, the infiltration of the melt begins under the influence of the applied pressure, which depends on the shape and size of the pore and their distribution, as well as the applied pressure.[18]

The infiltration kinetics in a bed of reinforcements is of importance to synthesize composites with enhanced mechanical properties. Most of analytical solutions for the infiltration kinetics were performed in a bed of fibers or irregularly shaped particles by considering factors, including threshold pressure, infiltration length, permeability, temperature distribution in the bed, and wettability between the melt and the particles.[19–31] Those factors are influenced by the size, temperature, and volume fraction of reinforcements, void size and distribution, melt temperature, melt flow patterns, and melt front conditions. Unlike a bed of fibers or irregularly shaped particles, a bed of spherical particles may have a relatively more uniform distribution of void sizes and distributions, which presumably can be advantages of synthesizing composites with high particle volume fractions.

Hollow particles in a metallic matrix lead to various advantages, including low density, high damping capacity, high thermal insulation, and high energy absorption.[32–35] The incorporation of hollow cenosphere particles in A356 alloys was observed to enhance the compressive properties.[36–38] Understanding and analysis of the infiltration kinetics in a bed of hollow particles are likely to lead to better processing conditions for synthesizing the composites with improved mechanical properties. Therefore, in this paper, pure aluminum melts were infiltrated into a loose bed of cenosphere spherical hollow fly ash particles and the infiltration characters were observed. An analytical model on infiltration of a bed of hollow spherical particles was proposed and compared with the experimental results. In fact, the analysis of the infiltration of a bed of fibers or irregular shape can be used to understand the infiltration kinetics of the bed of hollow spherical particles. However, the effect of hollow particles on

the infiltration kinetics will not be the same as that of fibers or solid particles. In general, the particles will be preheated at temperatures lower than the liquidus temperature of the matrix alloys. Thus, in the proposed analysis, the infiltration characters were analyzed for the particle temperatures lower than the liquidus temperature of pure aluminum melts. As a result, the solidified layers are expected to be formed on the particle surfaces. The apparent particle volume fraction due to the solidified layers was expressed in terms of the ratio of particle wall thickness and particle radius ($t/R$), and the effect of $t/R$ on the threshold pressure, pressure drop, melt temperature, melt viscosity, and melt velocity, and infiltration length were analyzed. This research will enable synthesis of new syntactic foams with very low porosity and defects using pressure infiltration by selection of optimum pressure as a function of the diameter, wall thickness, and temperature of the hollow particles.

## EXPERIMENTAL PROCEDURE

Hollow cenosphere fly ash particles were dried in an oven at 150–200°C in air. The chemical composition of hollow cenosphere particles used is shown in Table S1 in the supplementary materials. The major elements of hollow cenosphere particles are $SiO_2$ and $Al_2O_3$. The size of particles used in this study has an average diameter of 150 $\mu$m, and the particle wall thickness is in the range of 7 $\mu$m. Six-mm-diameter boro-silicate tubes were coated with zirconia coating to prevent the chemical reaction between the tube and the melt. The tubes containing cenosphere particles were packed and then tapped to improve the packing density of the samples. Both ends of the tube were sealed with Kaowool. Each tube was 18 mm OD, 16 mm ID, and 23 cm long. Then, the packed tubes were dried for at least 30 min in a heater at 250°C. The densities were of the order of 0.36 g/cm³. The packing density was calculated by measuring the net weight of cenosphere particles inside the borosilicate tube divided by the total length of cenosphere bed.

Pressure infiltration equipment (Figure S1 in the supplementary materials) consists of a stainless-steel chamber, which contains a resistance heater. Inside the chamber, a graphite-coated crucible rests on a refractory base. Pure aluminum ingots were placed in this crucible and melted at 800°C. At the melt temperature of 800°C, borosilicate tubes filled with fly ash particles were placed in the fitting on the lid of the infiltration set-up. The lid with the tube was then placed into the pressure chamber. The tube was preheated for 3 min at the chamber, and then various applied pressures in the range of 21 and 69 kPa were applied by introducing nitrogen gas into the pressure chamber for 3 min of infiltration time. The time for the system to reach the set pressure took approximately 5–10 s. After infiltration, the chamber was vented to cool the system,

and the sample was removed from the chamber. In this system, the minimum preheat time to achieve an isothermal condition at 700°C was found to be approximately 10 min. Therefore, it is expected that the particles in the tube do not have the same temperature as the melt.

The infiltrated length of samples was measured to determine its relationship to the applied pressure. The samples of the composite were sectioned at different locations along the length of the sample and mounted with dry phenoloic power and polished to observe the microstructure using a BH2-UMA optical microscope. Standard polishing procedures were followed using SiC grinding papers to 600 grit. Final polishing was done on a micropolishing cloth with a 0.05 mm $SiO_2$ slurry.

## MATHEMATICAL ANALYSIS

### Formation of a Solid Layer on the Particles

When the temperature of particles in a bed is lower than melt temperature, a solidified layer tends to form on the surface of the particles, as shown in Figure S2.[20] The layer will melt because of the flowing of hot melt.[20,37,39,40] The formation of the layer on the particles leads to a change in void size in the bed. The volume fraction of the solidified layer is related to the amount of heat absorbed by the particles from the liquid melt during the infiltration process. Heat exchange between the solid reinforcements and melt due to the formation of the solidified layer on the reinforcements is given by[24]

$$\varepsilon_p \rho_p C_p (T_l - T_p) = (1 - \varepsilon_p) \rho F H \quad (1)$$

where $\rho_p$ is the density of the particle; $\rho$ is the density of the melt; $C_p$ is the heat capacity of the particle; $C_l$ is the heat capacity of the melt; $T_l$ is the melt temperature; $T_p$ is the temperature of the particle; $H$ is the heat of melting; $\varepsilon_p$ is the volume fraction of the solid particle; $F$ is the eventual volume fraction of the solidified layer on the particle. In the case of hollow particles, Eq. 1 can be expressed in terms of the particle size and the wall thickness:

$$\varepsilon_p \left[ 1 - \left( 1 - \frac{t}{R} \right)^3 \right] \rho_p C_p (T_l - T_p) = (1 - \varepsilon_p) \rho F H \quad (2)$$

where $t$ is the wall thickness of the particles and R is the particle size. From Eq. 2, the volume fraction of the solidified layer can be obtained:

$$F = \frac{\varepsilon_p \left[ 1 - \left( 1 - \frac{t}{R} \right)^3 \right] \rho_p C_p (T_l - T_p)}{(1 - \varepsilon_p) \rho H} \quad (3)$$

In Eq. 3, it is shown that a lower $\rho_p$ and higher particle temperature result in a lower heat absolved by particles in a bed, resulting in a lower volume

fraction of the solidified layer. An increase in particle wall thickness is also likely to increase the solidified layer fraction. The apparent volume fraction of the particles due to the formation of the solidified layer is given by[24]

$$\varepsilon_p' = \varepsilon_p + (1 - \varepsilon_p) F \quad (4)$$

Substitution of Eq. 3 into Eq. 4 provides the apparent volume fraction, which depends on the ratio of particle wall thickness and the particle radius.

### Threshold Pressure

For a given system and applied pressure, the infiltration length becomes longer at a lower threshold pressure. Mortensen and Cornie[19] calculated the threshold pressure for a packed bed of solid spherical particles by considering the surface energy change due to the replacement of particle/vapor interfaces by the particle/melt interfaces. The threshold pressure for the infiltration of melt through a bed of spherical particles is given by[19]

$$P_{\text{th}} = -6\lambda \sigma_{\text{lv}} \cos \theta \frac{\varepsilon_p}{(1 - \varepsilon_p) d_p} \quad (5)$$

where $\sigma_{lv}$ is the surface energy of the particle and the melt; $\theta$ is the contact angle, $\varepsilon$ is the volume fraction of porosity of the bed, and $\lambda$ is the shape factor ($\lambda$ is 1 for spherical particle and 1.4 for angular particle). As the melt front advances and the solidified layer will form on the particles, the solidified layer on the particles does influence the threshold pressure with an increase in the apparent particle volume fraction. In the case the particle temperature influences the threshold pressure, Eq. 5 can be expressed in terms of the apparent particle volume fraction:

$$P_{\text{th}} = -6\lambda \sigma_{\text{lv}} \cos \theta \frac{\varepsilon_p'}{(1 - \varepsilon_p') d_p} \quad (6)$$

### Infiltration Length

During infiltration, as the melt infiltrates a bed of spherical particles, pressure drop occurs due to capillarity force and drag force acting on the surface of the particles, which can be expressed as,

$$\Delta P = \frac{\mu u}{k} l \quad (7)$$

where $\mu$ is the viscosity of the melt; u is the velocity of the melt; $l$ is the infiltration distance; and k is the permeability. The pressure drop $\Delta P$ is identical to the applied pressure minus the threshold pressure. When the particle temperature is lower than the melt temperature, the pressure drop depends on formation of the solidified layer on the particle. Due

to the formation of the solidified layer, the total pressure depends on the ratio ($\varphi$) of the length of the solidified layer to the total infiltration length. Therefore, the total pressure drop can be expressed in terms of $\varphi$ as follows:

$$\Delta P = \frac{\mu u}{k} l (1 - \phi) + \frac{\mu u'}{k'} l \phi \qquad (8)$$

where $u'$ and $u$ are the melt velocity at the regions with the solidified layers and without solidified layers, and $k'$ and $k$ are the permeability at the two regions, respectively. In this analysis $k'$ and $k$ are assumed to be identical due to the lack of data of those values.

In fact, the melt in the bed is not compressible and, therefore, the melt velocity in the bed of regions at the two regions can be expressed as follows:

$$u \left(1 - \varepsilon_p \right) = u' \left(1 - \varepsilon_p' \right) \qquad (9)$$

where $\varepsilon_p'$ is the apparent volume fraction of the particles. From Eqs. 8 and 9, the pressure drop can be expressed as,

$$\Delta P = \frac{\mu u}{k} l \left[ (1 - \phi) + \phi \frac{\left(1 - \varepsilon_p \right)}{\left(1 - \varepsilon_p' \right)} \right] \qquad (10)$$

During infiltration, the applied pressure on the melt front decreases with the melt front advancing. From Eq. 10, when the pressure at the melt front is equal to the threshold pressure, the advancement of the melt front can be assumed to be stopped,[24] and the total pressure drop at which the melt front stops can be expressed as follows;

$$\Delta P = P_{\text{app}} - \frac{4 \varepsilon_p \gamma \cos \theta}{d_p \left(1 - \varepsilon_p \right)} \qquad (11)$$

where $P_{\text{app}}$ is the applied pressure. Substitution of Eq. 11 into Eq. 10 leads to

$$P_{\text{app}} - \frac{4 \varepsilon_p \gamma \cos \theta}{d_p \left(1 - \varepsilon_p \right)} = \frac{\mu u}{k} l \left[ (1 - \phi) + \phi \frac{\left(1 - \varepsilon_p \right)}{\left(1 - \varepsilon_p' \right)} \right] \qquad (12)$$

Integrating Eq. 12, the infiltration length can be expressed as the square of the infiltration length as a function of time t and the pressure drop $\Delta P$;

$$l = (At)^{1/2} \qquad (13)$$

where

$$A = \frac{2 k \Delta P}{\mu \left[ (1 - \phi) + \phi \frac{\left(1 - \varepsilon_p \right)}{\left(1 - \varepsilon_p' \right)} \right]}$$

where

In Eq. 12, the infiltration length depends on the apparent particle volume fraction due to the formation of the solidified layers on the particles. The term A in Eq. 12 is similar to $\Psi$,[19] which is equal to $\left[ \frac{2 k \Delta P}{\mu \left(1 - V_f \right)} \right]^{1/2}$, where $V_f$ is the fiber volume fraction.

## RESULTS AND DISCUSSION

### Microstructure

The stacking of the particles in the tube forms voids between particles; smaller channels are near the contact area between the particles and larger voids. During infiltration, the capillary resistance is very high in the narrow channel near interparticle contact regions, where much higher applied pressure is required for the flow of the metal through this channel compared to a larger void. Therefore, larger voids are at first filled by the melt, and then the smaller ones are filled. The microstructures from (1) The bottom and (2) The top of aluminum-containing spherical cenosphere particles, infiltrated at an applied pressure of 34 kPa for 3 min of infiltration time, are shown in Fig. 1a and b. This figure shows that the larger voids are infiltrated by the melt, the high volume fraction of the particles is uniformly distributed in the matrix, and their volume fraction or hollow particles is around 65%.

The bed of loosed particles is infiltrated at an applied pressure which is higher than the threshold pressure. It can be also noted from Fig. 1 that the applied pressure of 34 kPa is higher than the threshold pressure, above which the melt starts to flow into the voids between particles. Figure 1 also shows that there are some porosities near the contact area of cenosphere particles. This indicates that an applied pressure of 34 kPa is not high enough for the flow of the melt through the channel, resulting in the formation of the pore in some interparticle regions. The presence of pores between the fibers can be observed because of high capillarity pressure at the contact regions between the fibers.[19,22]

The microstructure near the bottom of the aluminum rod containing cenosphere particles, infiltrated at an applied pressure of 69 kPa for 3 min of infiltration time, is shown in Figure S3. This figure shows uniform distribution of the particles and their high volume fraction in the matrix as well as the presence of pores near the particle contacts. The presence of the pore near the contact surfaces between the particles indicates that the applied pressure of 69 kPa is also not high enough to fill the pore between the particles.

### Infiltration Length

The variation of the infiltration length with applied pressure in pure aluminum containing spherical cenosphere particles (average diameter $150 \mu m$) was measured at applied pressures varying
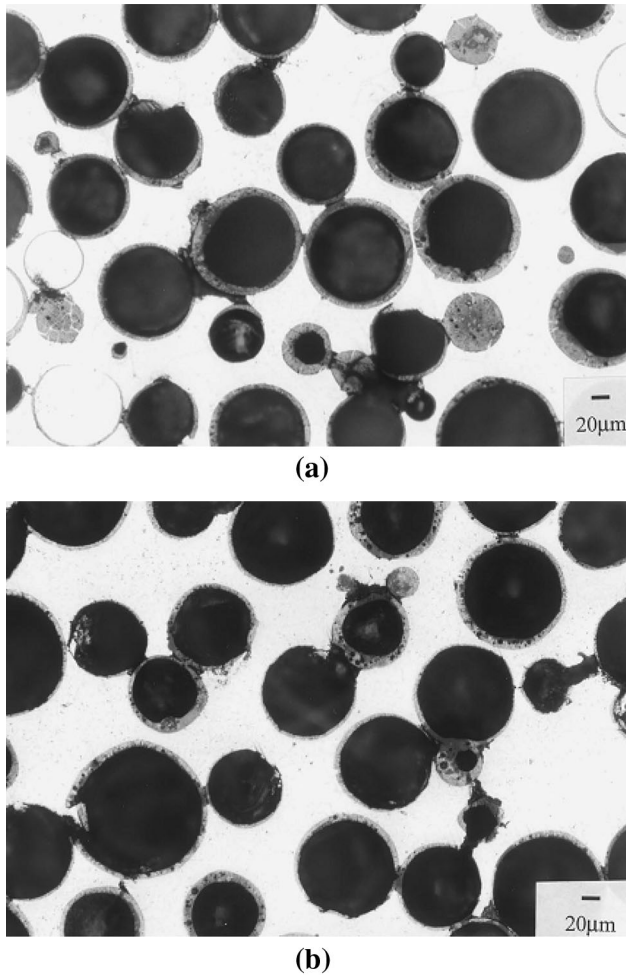
**(a)**



**(b)**

Fig. 1. Microstructure of (a) the bottom and (b) the top portion of aluminum containing cenosphere particles, infiltrated at an applied pressure of 34 kPa.



Fig. 2. Variation of infiltration length with the applied pressure for beds of an average 150 $\mu$m diameter of fly ash hollow particles for 3 min of infiltration time.



Fig. 3. Calculated variation of the volume fraction of a solidified layer on the particles; $t = 7$ $\mu$m, $R = 75$ $\mu$m, and $\varepsilon_p = 0.65$.

from 21 to 69 kPa and is shown in Fig. 2. The infiltrated length increases rapidly at applied pressures between 28 and 34 kPa and increases gradually at applied pressures > 34 kPa. The threshold pressure is likely to be in the range of 28 and 34 kPa. The threshold pressure calculated using Eq. 5 is 48 kPa, which is higher than the experimentally measured value (in the range 28 and 34 kPa). In fact, the distribution of the particles in the bed is not uniform and therefore the melt is infiltrating into the voids with larger size and then into the smaller size. Therefore, the measured threshold pressure does not agree with the calculated one. Another reason for the disagreement is presumably the variation in particle size. An average particle size used in this study is 150 $\mu$m. However, the presence of the particles with a different size leads to a non-uniform distribution of particle size.

## Effect of the Solidified Layer

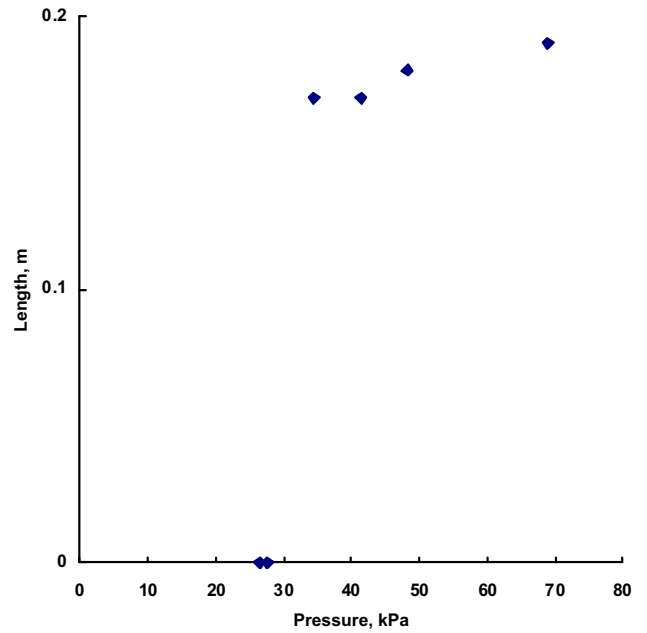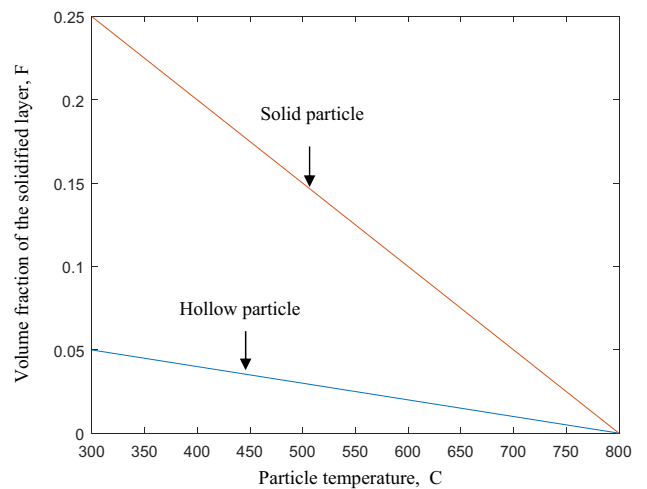During infiltration, the particle temperature influences the infiltration length due to the formation of solidified layers on the surface of the particles. The effect of the particle temperature on the solidified volume fraction on the particle temperature is shown in Fig. 3, which is plotted using Eq. 3 and the data shown in Table I. It is shown that the volume fraction of the solidified layers increases with decreasing particle temperature and more solidified layers are formed on the solid particles as compared to the hollow particles. This is likely to be because more heat can be absorbed by the solid particles than the hollow particles and that lower particle temperatures can also cause a larger amount of heat absorbed by both particles to form solidified layers as compared to higher particle temperatures.

**Table I. Thermophysical properties of A356 aluminum melt and fly ash cenosphere hollow particle**

| Parameters | Description | Magnitude | Refs. |
|---|---|---|---|
| $H$ | Latent heat | 397 kJ/kg | 41 |
| $C_p$ | Heat capacity of fly ash | 0.7 kJ/kg | 42 |
| $C_l$ | Heat capacity of aluminum melt | 1.09 kJ/kg | 41 |
| $\rho_p$ | Hollow cenosphere density | 360 kg/m$^3$ | 43 |
| $\rho$ | Density of aluminum melt | 2375 kg/m$^3$ | 41 |
| $\mu$ | Viscosity of aluminum melt | $2.9 \times 10^{-3}$ kg/m.s | 41 |
| $\sigma_{lv}$ | Surface tension of liquid/vapor | 1.1 N/m | – |
| $T_m$ | Melting temperature of pure aluminum melt | 660°C | 41 |
| $T_l$ | Aluminum melt temperature | 800°C | 19 |

Figure 3 shows that the difference in the solidified layer between the solid and hollow particles is shown to decrease with increasing particle temperature. This means that, at lower particle temperatures, the melt infiltration in a bed of hollow particles is more favorable than in a bed of solid particles. One advantage of hollow particles is that the volume fraction of the solidified layers on hollow particles at a particle temperature of 500°C is obtained at a bed of solid particles preheated at 750°C. Therefore, a higher preheated particle temperature is necessary in a bed of solid particles compared to a particle temperature in a bed of hollow particles.

As observed in Fig. 3, which shows lower solidified layer amounts on hollow particles than solid particles, the number of solidified layers on the hollow particles is expected to vary with particle wall thickness, since the amount of heat absorbed by a hollow particle depends on its wall thickness for a given particle size. This tendency is shown in Fig. 4; the solidified volume fraction increases with increasing $t/R$ at the two particle temperatures of 300°C and 600°C. This figure also illustrates the effect of particle temperature on the solidified layer volume fraction, i.e., the volume fraction is higher at the lower particle temperature of 300°C than at the higher particle temperature of 600°C. These results are associated with the fact the heat absorbed by the particles is greater when the particle temperature is lower and the particle is thicker, which leads to a lower solidified volume fraction. In addition, Fig. 4 shows that the difference in solidified volume fraction formed on the particles at the two particle temperatures increases with increasing particle wall thickness. As a result, higher particle temperatures are required for better infiltration of a bed of solid particles.

The apparent volume fraction of solidified layers on particles, plotted as a function of the ratio of particle wall thickness and particle radius ($t/R$), are illustrated in Fig. 5a and b. The apparent volume fraction is shown to increase with $t/R$ and to be larger at a particle temperature of 300°C than at a particle temperature of 600°C. These results are associated with the dependence of heat absorbed by
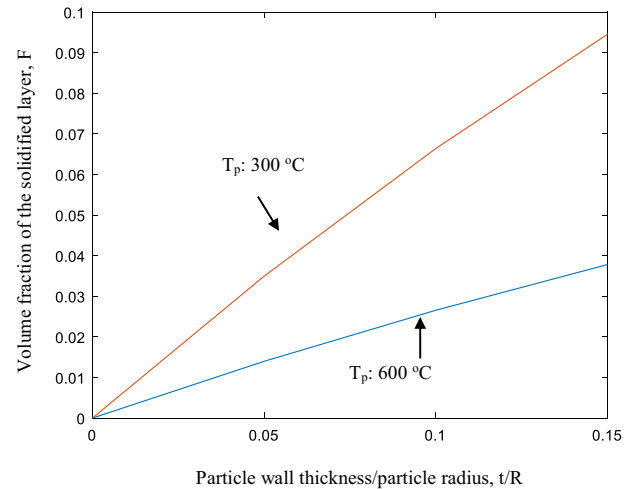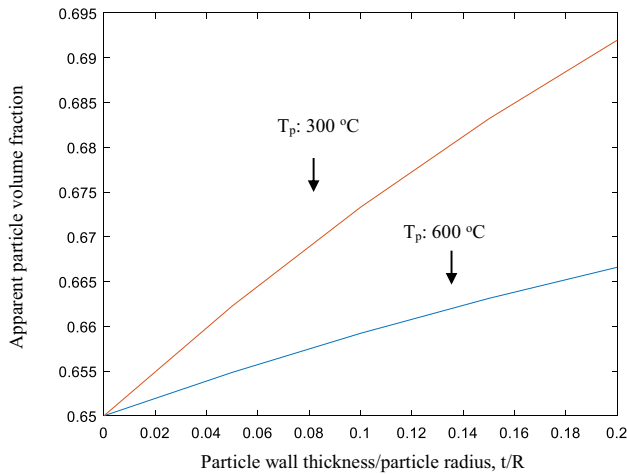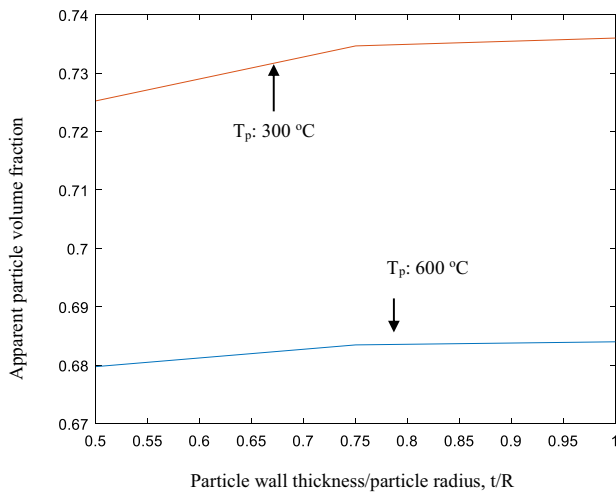


**(a)**
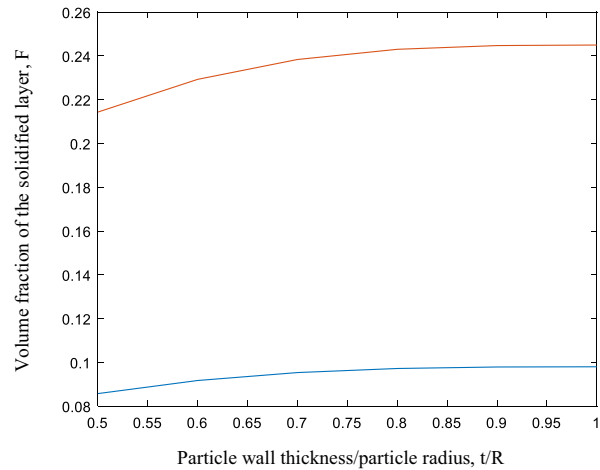


**(b)**

Fig. 4. Variation of the volume fraction of a solidified layer on the particles with the ratio of particle wall thickness and particle radius ($t/R$); R = 75 $\mu$m and $\varepsilon_p$ = 0.65, (a) $t/R$ = 0.0–0.15, (b) $t/R$ = 0.5–1.

the particles on $t/R$ and particle temperature, as explained before. The difference in apparent volume fraction at the two temperatures is also shown to decrease with t/R. This result suggests that thinner

**(a)**



**(b)**

Fig. 5. Variation of the apparent particle volume fraction as a function of the ratio of particle wall thickness to particle radius, (a) $t/R$ = 0.0–0.2, (b) $t/R$ = 0.5–1.



Fig. 6. Variation of threshold pressure as a funtion of the ratio of particle wall thickenss and particle radius at two different particle temperatures of 300°C and 600°C and two contact angles of $\theta = 130^{\circ}$ and $\theta = 127^{\circ}$.

hollow particles are less sensitive to the particle temperature on the formation of the solidified layer. However, as $t/R$ increases, the effect of particle temperature on the solidified layer increases. For $t/R$ = 0.09, i.e., the ratio of the particle wall thickness and the particle diameter for the current system, as shown in Fig. 5a, the apparent volume fractions are 67.3% and 65.7% at the two particle temperatures of 300°C and 600°C, respectively. The difference in the apparent particle volume fraction for the two temperatures is around 2%. For $t/R$ = 1, as Fig. 5b shows, the apparent particle volume fractions are 73.7% and 68.5% for the two particle temperatures, and the difference in apparent particle volume fraction is around 5%. This result suggests that as particle wall thickness increases, the apparent particle volume fraction is more sensitive to particle temperatures. Therefore, for a bed of solid particles,
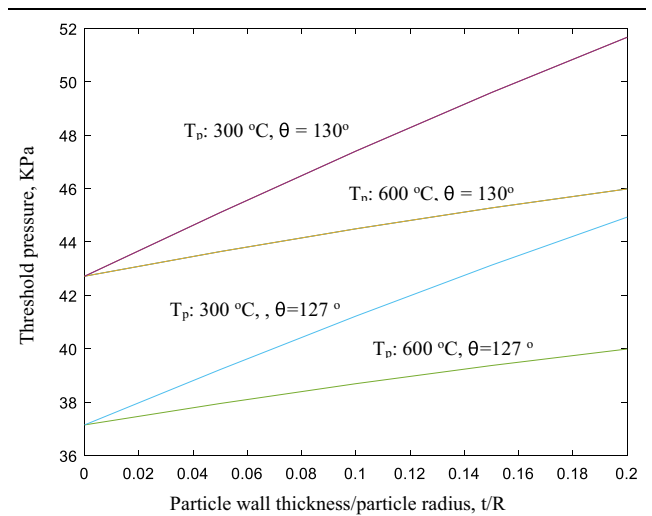
higher particle temperatures are required for improved infiltration. The infiltration length has been reported to increase with increasing preheat temperature of solid particles.[22,44]

During infiltration, the formation of solidified layers on the particles, which depends on particle temperature and $t/R$, influences the threshold pressure. The effects of particle temperature and t/R on the threshold pressure are illustrated in Fig. 6, for two different particle temperatures of 300°C and 6000°C and two different contact angles, i.e., 127° and 130°. The threshold pressure is shown to increase with increasing $t/R$ and with decreasing particle temperatures. This result can be related to the apparent volume fraction, as shown in Fig. 4, which depends on $t/R$ and particle temperatures. Since increasing $t/R$ and decreasing particle temperatures result in an increase in apparent particle volume fraction, the threshold pressure is greater at a thicker particle wall and a lower particle temperature. Figure 6 shows that as $t/R$ decreases, the difference in threshold pressure decreases for the two particle temperatures, which means that for thin wall particles, the effect of particle temperature on the threshold pressure is less compared to solid particles. This is related to the fact that the apparent particle volume fraction becomes less sensitive to particle temperatures with decreasing $t/R$, since the amount of heat absorbed by the particles becomes less sensitive to particle temperature with deceasing $t/R$.

Upon ignoring the effect of solidified layers on the threshold pressure, the threshold pressure was calculated using Eq. 5. The contact angle between a cenosphere particle and pure aluminum melt is not available. As can be seen in Table S1, cenosphere particles consist of various elements, and the major elements are $SiO_2$ and $Al_2O_3$. Therefore, the

contact angle value $\theta$ between a cenosphere particle and pure aluminum melt was calculated based on the volume fraction of the two elements of $SiO_2$ and $Al_2O_3$, using the contact angle value between pure aluminum melt and $SiO_2$ or $Al_2O_3$ (Table II). With the calculated $\theta$ value of 130°, the threshold pressure is calculated to be 42.7 kPa. For hollow cenosphere particles used in the current experiment, at which $t/R$ = 0.09 (the cenosphere wall thickness and radius are 2 $\mu$m and 75 $\mu$m) and at preheat particle temperatures of 300° and 600°C, the threshold pressures are 44 and 42 kPa, respectively (Fig. 6). These calculated values are higher than the measured threshold pressure which appears to be close to 35 kPa (Fig. 2). In fact, Eq. 5 is derived under the condition of a uniform particle distribution in the bed; however, the particle distributions are not uniform and, therefore, the melt will flow into the larger voids preferentially, which will cause deviation of the calculated value from the measured value.

In fact, in this analysis, the measured $\theta$ value between a cenosphere particle and pure aluminum melt is not available. As shown in Fig. 6, when the $\theta$ decreases by 3 degrees from 130° to 127°, the threshold pressures at $\theta$ = 127° are lower than those at $\theta$ = 127° at the two different temperatures. At $t/R$ = 0.09, the threshold pressures at the two temperatures are 38 and 40 kPa, respectively, which is closer to the measured threshold pressure range of 28 and 34 kPa. Therefore, it is important to identify more accurate values of particle temperatures and measure contact angle values. In addition, when the particle temperature is higher than 600°C, the threshold pressure is much closer to the measured value.

In reality, a nonuniform distribution of particle and void size variations may contribute to the deviation of the calculated value from the measured values. During infiltration of a bed of fibers, non-uniform distribution of interspaces between the fibers leads to the melt infiltration into the larger interspaces,[22] which will happen in a bed of hollow spherical particles. The particles also can move because of the melt infiltration, causing the change in the void distributions and sizes. In addition, the morphology, surface topology, and specific surface area of the particles are crucial factors for identifying a more reliable threshold pressure.[27,47] These

effects can result in a deviation of the calculated results from the measured values in the infiltration processes.

As shown in Eq. 9, during infiltration, the melt flow is expected to be influenced by the formation of solidified layers on the particles and, therefore, the melt velocities in solidified layer ($u'$), and the nonsolidified layers ($u$) regions will be different. The ratio of the melt flow velocity in the two regions ($u'/u$) was plotted as a function of t/R in Fig. 7. It is shown that, for $t/R$ = 0.09 and two particle temperatures of 300°C and 600°C, the $u'/u$ is slightly lower at the higher particle temperature of 600°C, but the $u'/u$ values for the two temperatures are in the range 0.97 and 0.96, respectively. This result indicates that the melt flow velocity can be assumed to be identical at the two regions, since the amount of the solidified layer is small enough so that the melt flow is not significantly influenced by the solidified layer. However, for $T_p$ = 300°C and $t/R$ = 1, the $u'/u$ value is 0.76, which suggests that the particle wall thickness effect is greater at lower particle temperatures and at thicker particle walls because of an increase in apparent volume fraction with decreasing particle temperatures and increasing $t/R$. Therefore, it is necessary to consider the particle wall thickness effect at a certain apparent volume fraction above which the melt velocities at the two regions are different enough to influence the total infiltration length.

In this analysis, the permeability values at the two regions are assumed to be identical. In Eq. 12, it can be noted that the infiltration length depends on the permeability at the two regions. The permeability ($k$) was calculated using the Carman-Kozeny model[48]: $k = \frac{\varepsilon^3 d_p^2}{36K(1-\varepsilon)^2}$, where $\varepsilon$ is the void fraction of the bed, $d_p$ is the particle diameter, and K is 1.7. The calculated k value of the current system is 1.06 $\times$ $10^{-10}$ m$^2$. In the above equation, it can be noted that $k$ strongly depends on the void fraction. From Fig. 5, it can be noted that the apparent particle volume fractions are 0.67 and 0.66 for the two particle temperatures of 300°C and 600°C and $t/R$ = 0.09, respectively (Fig. 5). The volume fraction increase because the solidified layer formation is 0.2 and 0.1 for the two temperatures and, therefore, the permeability in the solidified layer regions is expected to be very similar to that in the

**Table II. Wetting angles of selected ceramics with molten aluminum[45,46]**

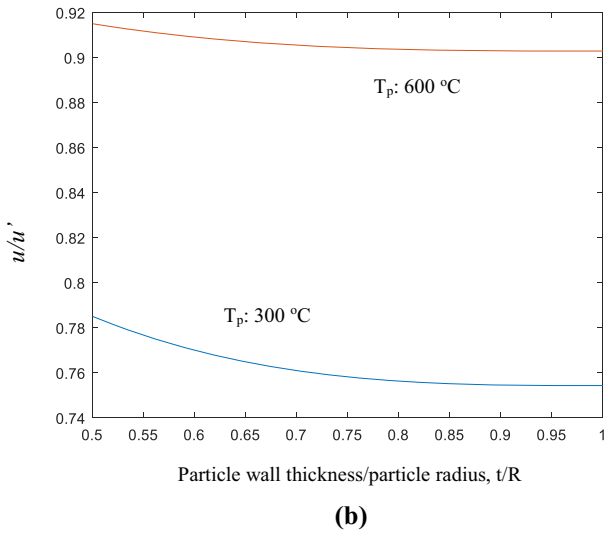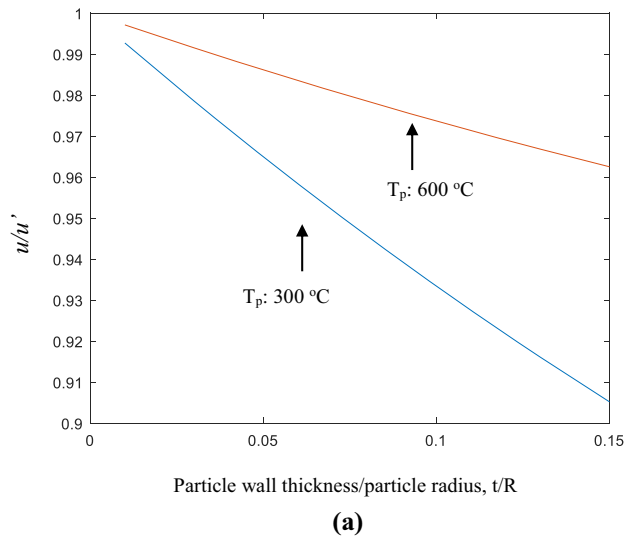| Ceramic | Temperature,°C | Average wetting angle, degree |
| --- | --- | --- |
| SiC | 870 | 150 |
| $SiO_2$ | 800 | 135 |
| $Al_2O_3$ | 800 | 115 |

**(a)**



**(b)**

Fig. 7. Variation of *u/u'* as funtion of the ratio of particle wall thickenss and particle radius (t/R) at two different particle tempertures of 300°C and 600°C, (a) *t/R* = 0.0–0.15, (b) t/R = 0.5–1.



Fig. 8. Variation of dimentioanless pressure drop with the apparent particle volume fraction.

unsolidified layer regions, when particle wall thickness is small. However, with increasing particle wall thickness, the apparent particle volume fraction effect on k' will increase because of a decrease in void fraction with an increase in apparent particle volume fraction. Therefore, there will be a critical apparent particle volume fraction, above which apparent particle volume fractions need to be considered for calculating $k$. In addition, during the infiltration of the melt into fibers, fiber deformation occurs,[24,39] which can cause a change in $k$. In a bed of loosened particles, the particles can be pushed apart because of the melt flow around the particles, which can lead to change in k.

The ratio $\varphi$ of the length of a solidified layer region and a non-solidified layer region influences the total infiltration length because of the melt flow difference in the two regions, as can be seen in
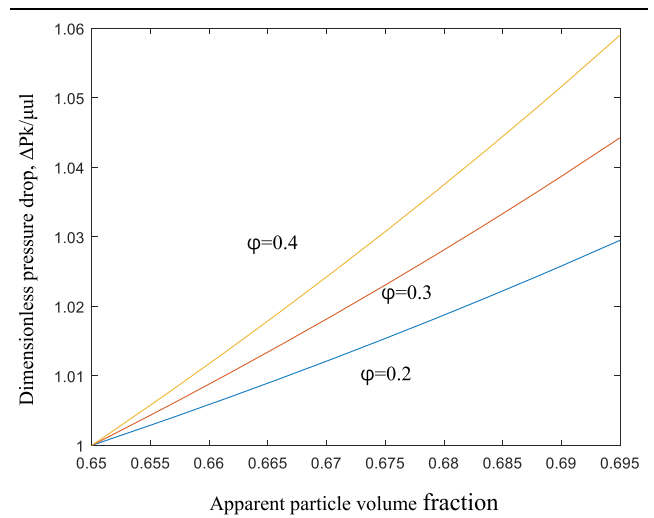
Eq. 12. Equation 12 also illustrates that the total infiltration length depends on the pressure drop ΔP, which is influenced by the apparent volume fraction. Figure 8 shows the effect of apparent volume fraction on the dimensionless pressure drop (ΔP$k$/$\mu u l$) for the three different values of $\varphi$, i.e., 02, 03, and 0.4. In fact, the $\varphi$ value is not available; therefore, the three arbitrary $\varphi$ values were used. Figure 8 shows that the dimensionless pressure drop increases with increasing apparent volume fraction and $\varphi$. This is because as the apparent volume fraction and $\varphi$ increases, the voids through which the melt flows decrease, which causes an increase in pressure drop. The rate of an increase in the dimensionless pressure drop is also shown to increase with increasing $\varphi$. Therefore, the effect of $\varphi$ on the pressure drop is smaller at small apparent volume fraction. Since the apparent volume fraction is smaller at smaller $t/R$, hollow particles with thinner particle walls have a less effect of $\varphi$ on the pressure drop.

As Fig. 5 shows, the apparent volume fractions are 67% and 65.7% at particle temperatures of 300°C and 600°C at $t/R$ = 0.09. Figure 9 shows that the dimensionless pressure drops at the two apparent volume fractions are around 1.01 for the three $\varphi$ values, even though the pressure drop is lowest at $\varphi$ = 0.2. For $t/R$ of < 0.09, the effect of on the pressure drop is expected to be much smaller. This result shows that the effect of $\varphi$ on the pressure drop is very small in the case of a bed of hollow particles with thin particle walls. However, the pressure drop increases with increasing $\varphi$; therefore, there will be a critical value of $\varphi$ above which the melt flow at solidified layer regions is important for the infiltration kinetics.

During infiltration, the infiltration length varies with t, as can be seen from Eq. 12. The variation of infiltration length with time at the applied pressure of 69 kPa and at two different t/R values of 0.09 and
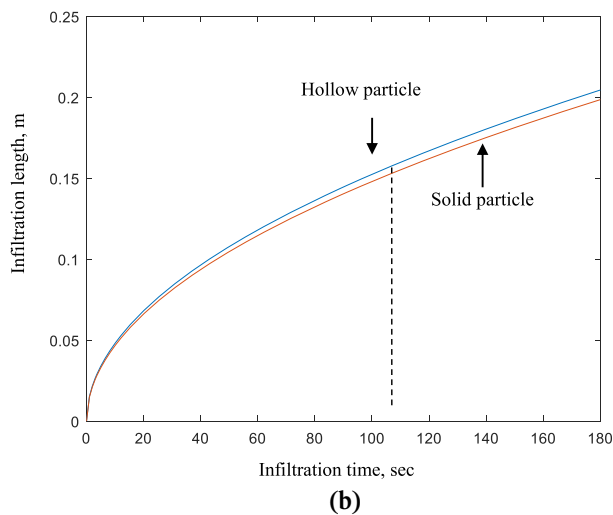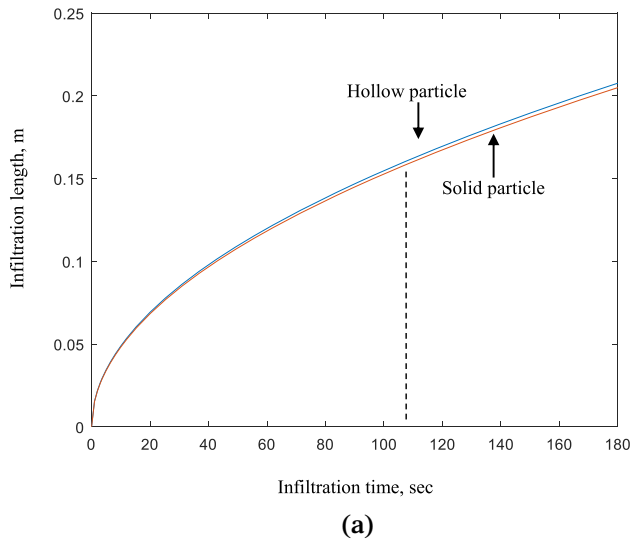
Fig. 9. Variation of infiltration length with infiltration time at 69 kPa. (a) $T_p$ = 600°C and t/R = 0.09 (b) $T_p$ = 300°C and t/R = 1.
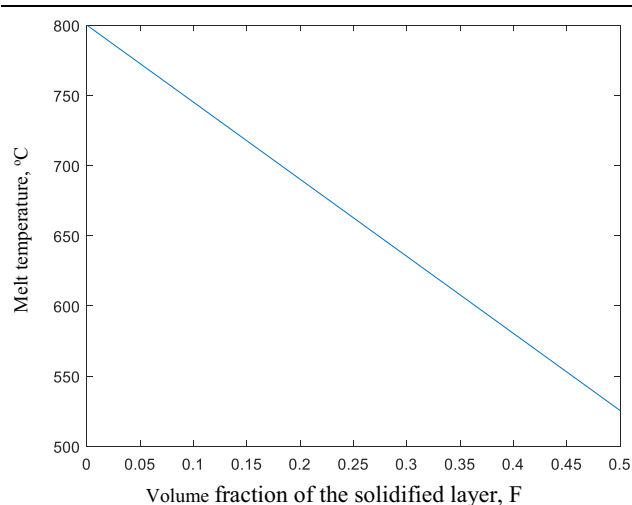


Fig. 10. Variation of melt temperature with the volume fraction of the solidified layers.

1 is shown in Fig. 10. The curves show a parabolic dependence of infiltration length on time.[20,27] The infiltration lengths are illustrated to be longer at the higher particle temperature of 600°C and for the lower $t/R$ of 0.09. Mortensen et al.[20] and Castro[49] reported the effect of fiber temperature on infiltration; the infiltration length increases with increasing fiber temperatures. However, Fig. 10 shows that the difference in infiltration length due to hollow particles and solid particles is not pronounced. In fact, in this analysis, the effect of the melt viscosity changes on the infiltration length because heat absorbed by the particles was not considered. When this effect is considered, the difference in the infiltration length between a bed of the hollow and a bed of solid particles is likely to be more pronounced.

During melt infiltration, the melt temperature around solidified layers on the particles depends on the number of solidified layers. The melt temperature due to the formation of the solidified layer can be expressed as follows; $T = T_l - \frac{F}{C_l}[H + C_l(T_l - T_m)]$. Figure 10 shows the variation of melt temperature with the volume fraction of solidified layers. For $t/R$ = 0.09 at which the solidified layers volume fractions are 0.672 and 0.657 for particle temperatures of 300°C and 600°C (Fig. 4), as shown in Fig. 10, the melt temperature is decreased from the initial melt temperature of 800°C to 760°C at a particle temperature of 300°C and to 790°C for a particle temperature of 600°C, respectively. For $t/R$ = 1, the melt temperature changes due to the solidified layer formation will be greater than for $t/R$ = 0.09. The calculation shows that the temperature is decreased from 800°C to 670°C and to 740°C for particle temperatures of 300°C and 600°C, respectively. This result is due to the fact that more solidified layers are formed at the at lower particle temperatures and at thicker particle walls.

The decrease in melt temperature causes an increase in the melt viscosity, which leads to a decrease in infiltration length. Since solidified layers are less around thin wall particles, the melt viscosity around the particles will be relatively lower than that around solid particles. Therefore, a bed of hollow particles can have a longer infiltration length than that of solid particles. In fact, there will be a case where, with the melt front advancing a certain distance, the melt temperature will be lower than the liquidus temperature because of the solidified layer formation so that the melt will flow at the semi-solid state.[19,36,40,50] Nicom et al. observed a rapid decrease in permeability with increasing the solid fraction in the semi-solid range,[51] and Yu et al. suggested the importance of wetting conditions and viscosity during infiltration due to a rapid change in viscosity and wetting with temperature.[52] Therefore, when the temperature of the melt front decreases with the melt front

advancing, it is necessary to consider the effect of the change in viscosity and permeability of the melt together to obtain more accurate values of the infiltration length with time.

On the other hand, a suitable coating which reduces the contact angle between the particle and the melt is helpful in improving infiltration length and reducing threshold pressure. Murthy et al. observed the improvement in infiltration kinetics of Al due to an improved wettability of SiC particles by the Cu and Ni coatings.[44] The pores present near the contact area of the particles can also be filled more easily by the melt when wettability between the melt and the particle is lower. Therefore, the treatment of the particle to improve wettability between the melt and the particles will lead to a decrease in the content of pores present in inter-particle contact regions.

In this analysis, the value of the contact angle between the pure aluminum melt and the particle obtained from the sessile drop experiment under static conditions was used. In fact, since the particles in the melt are moving, the contact angle between the melt and the particle could be different from the contact angle under dynamic contact conditions than what is measured under static conditions. In general, the contact angle also decreases with increasing temperature.[53,54] With the melt front advancing, the contact angle between the melt and the particles is likely to change because of the change in the melt front temperature. The decrease in the melt temperature with increasing infiltration length can increase melt viscosity. As a result, it is necessary for the changes in the contact angle and melt viscosity at the melt front with the front moving to be considered to identify more accurate characteristics of melt infiltration in the bed of particles. In reality, the infiltration process is expected to be influenced to some extent by the shape and size of the voids, which will lead to side melt flow and affect the drag force acting on the surface of the particles. Therefore, understanding the flow patterns in the voids will result in identifying the characters of the melt infiltration in a bed of spherical hollow with more accuracy.

## CONCLUSION

Pure aluminum melts were infiltrated into a loose bed of hollow spherical cenosphere particles. The infiltration increases gradually at applied pressures > 35 kPa. The threshold pressure is likely to be in the range of 28 and 35 kPa. The estimated threshold pressure is higher than the measured threshold pressure, presumably due to the uncertainty in contact angle value $\theta$ between cenosphere particles and pure aluminum melt and nonuniform distribution of particles and voids.

The volume fraction of a solidified layer, F, on the cenosphere hollow particles increased with decreasing particle temperatures and increasing the ratio of particle wall thickness and particle radius ($t/R$). The apparent volume fraction also showed the same dependence of the particle temperature and $t/R$ as observed in F. Hollow particles and particles with higher temperatures absorb less heat from the melt compared to solid particles and particles with higher temperatures, which leads to a less apparent particle volume fraction. Therefore, hollow particles with higher temperatures will improve infiltration kinetics by reducing the threshold pressure, permeability, melt velocity in solidified layer and unsolidified layer regions, dimensionless pressure drop, and melt temperature around the particles as compared to solid particles with lower temperatures. Hollow particles have an advantage over solid particles for lower particle temperatures; the formation of apparent particle volume fraction becomes less sensitive to particle temperatures with decreasing $t/R$.

The flow of the melt in the various sizes and shapes of the voids will lead to melt flow to the sides and affect the drag force acting on the surface of the particles. Thus, it influences permeability and the melt flow pattern. Nonuniform distribution of the voids and particles may cause the measured threshold pressure value to deviate from the calculated values, which assumes a uniform particle distribution and an unavailability of the measured contact angle value between the cenosphere particle and pure aluminum melt. The effect of melt temperature changes with the melt front advancing because of the formation of the solidified layers on the flow patterns in the voids needs to be considered for identifying the characteristics of the melt infiltration in a bed of spherical hollow with more accuracy. This type of research will lead to better estimation of infiltration behavior of melts into beds of hollow ceramic particles and synthesis of improved syntactic foams with wider application.

## DATA AVAILABILITY

Data will be made avilable on reasonable request.

## CONFLICT OF INTEREST

All authors declare no conflict of interest.

## SUPPLEMENTARY INFORMATION

The online version contains supplementary material available at https://doi.org/10.1007/s11837-022-05226-y.

# REFERENCES

1. A. Kordijazi, T. Zhao, J. Zhang, K. Alrfou, and P. Rohatgi, *JOM* 73, 2060 (2021).
2. P.K. Rohatgi, R. Asthana, and S. Das, *Int. Metals. Rev.* 31, 115 (1986).
3. A. Mortensen, and I. Jin, *Int. Mater. Rev.* 37, 101 (1992).
4. M. Ravichandran, M. Meignanamoorthy, G.P. Chellasivam, J. Vairamuthu, A. Senthil Kumar, and B. Stalin, *Mat. Today: Proc.* 22, 2606 (2020).
5. R. Asthana, and S.N. Tewari, *J. Mater. Sci.* 28, 5414 (1993).
6. N. Setargew, B.A. Parker, and M.J. Couper, *The settling of reinforcement particles during the casting of aluminium-silicon base MMCs* (Metals and Materials Society, Warrendale, PA (United States, Minerals, 1993).
7. P.K. Rohatgi, P. Ajay Kumar, N.M. Chelliah, and T.P.D. Rajan, *JOM* 72, 2912 (2020).
8. J.K. Kim, and P.K. Rohatgi, *Metall. Mater. Trans. A.* 29, 351 (1998).
9. J.K. Kim, and P.K. Rohatgi, *Acta Mater.* 46, 1115 (1998).
10. S. Das, A. Kordijazi, O. Akbarzadeh, and P. K. Rohatgi, Engineering Reports e12110 (n.d.).
11. J. Tian, E. Piñero, J. Narciso, and E. Louis, *Scripta Mater.* 53, 1483 (2005).
12. A. Alonso, A. Pamies, J. Narciso, C. Garcia-Cordovilla, and E. Louis, *Metall. Mater. Trans. A* 24, 1423 (1993).
13. J. Zhu, F. Wang, Y. Wang, B. Zhang, and L. Wang, *Ceram. Int.* 43, 6563 (2017).
14. H.S. Lee, and S.H. Hong, *Mater. Sci. Technol.* 19, 1057 (2003).
15. S. Elomari, R. Boukhili, C. San Marchi, A. Mortensen, and D.J. Lloyd, *J. Mater. Sci.* 32, 2131 (1997).
16. E. Candan, H. Ahlatci, and H. Cimenoglu, *Wear* 247, 133 (2001).
17. S. Candan, *Mater. Lett.* 58, 3601 (2004).
18. D.B. Newsome, B.F. Schultz, J.B. Ferguson, and P.K. Rohatgi, *Materials* 8, 6085 (2015).
19. A. Mortensen, and J.A. Cornie, *Metall. Mate.r Trans. A* 18, 1160 (1987).
20. A. Mortensen, L.J. Masur, J.A. Cornie, and M.C. Flemings, *Metall. Mater. Trans. A* 20, 2535 (1989).
21. S. Nourbakhsh, F.-L. Liang, and H. Margolin, *Metall. Mater. Trans. A* 20, 1861 (1989).
22. S. Long, Z. Zhang, and H.M. Flower, *Acta. Metall. Mater.* 42, 1389 (1994).
23. D. Muscat, and R.A.L. Drew, *Metall. Mater. Trans. A* 25, 2357 (1994).
24. T. Yamauchi, and Y. Nishida, *Acta. Metall. Mater.* 43, 1313 (1995).
25. C. Garcia-Cordovilla, E. Louis, and J. Narciso, *Acta Mater.* 47, 4461 (1999).
26. V. Michaud, and A. Mortensen, *Scripta Mater.* 56, 859 (2007).
27. G. Kaptay, *Compos. Sci. Technol.* 68, 228 (2008).
28. I.N. Orbulov, *Mater. Sci. Eng., A* 583, 11 (2013).
29. J.A. Santa Maria, B.F. Schultz, J.B. Ferguson, and P.K. Rohatgi, *Mater. Sci. Eng: A* 582, 415 (2013).
30. J.B. Ferguson, J.A. Santa Maria, B.F. Schultz, and P.K. Rohatgi, *Mater. Sci. Eng: A* 582, 423 (2013).
31. J.E. Rivera-Salinas, K.M. Gregorio-Jáuregui, A. Cruz-Ramírez, J.A. Romero-Serrano, E. Ramírez-Vargas, V.H. Gutierréz-Pérez, and L.F.J. Hernández-Quintanar, *Metall. Mater. Trans. A* 52, 826 (2021).
32. P.K. Rohatgi, N. Gupta, B.F. Schultz, and D.D. Luong, *JOM* 63, 36 (2011).
33. N. Gupta, and P.K. Rohatgi, *Metal matrix syntactic foams: processing, microstructure properties and applications* (DEStech Publications Inc, USA, 2014).
34. A. Szlancsik, B. Katona, A. Kemény, and D. Károly, *Materials* 12, 2023 (2019).
35. I.N. Orbulov, A. Szlancsik, A. Kemény, and D. Kincses, *Compos. Part A: Appl Sci Manuf.* 135, 105923 (2020).
36. P.K. Rohatgi, J.K. Kim, N. Gupta, S. Alaraj, and A. Daoud, *Compos. A Appl. Sci. Manuf.* 37, 430 (2006).
37. V.J. Michaud, and A. Mortensen, *Metall. Mater. Trans. A* 23, 2263. (1992).
38. N. Wang, X. Chen, Y. Li, Y. Liu, H. Zhang, and X. Wang, Materials Transactions **advpub**, (2018).
39. P. Jarry, V.J. Michaud, A. Mortensen, A. Dubus, and R. Tirard-Collet, *Metall. Mater. Trans. A* 23, 2281 (1992).
40. E.S. Eardley, and H.M. Flower, *Mater. Sci. Eng., A* 359, 303 (2003).
41. J.F. Shackelford, Y.-H. Han, S. Kim, and S.-H. Kwon, *CRC materials science and engineering handbook* (CRC Press, Florida, 2016).
42. D. D. Luong, N. Gupta, and P. K. Rohatgi, in *Advanced Carbon Materials and Technology* (John Wiley & Sons Ltd, 2014), pp. 377–417.
43. C. Garcia-Cordovilla, E. Louis, and A. Pamies, *J. Mater. Sci.* 21, 2787 (1986).
44. B.S. Murty, S.K. Thakur, and B.K. Dhindaw, *Metall. Mater. Trans. A* 31, 319 (2000).
45. V. Laurent, D. Chatain, and N. Eustathopoulos, *J. Mater. Sci.* 22, 244 (1987).
46. J.J. Brennan, and J.A. Pask, *J. Am. Ceram. Soc.* 51, 569 (1968).
47. J.M. Molina, R. Prieto, M. Duarte, J. Narciso, and E. Louis, *Scripta Mater.* 59, 243 (2008).
48. M. Mota, J.A. Teixeira, W.R. Bowen, and A. Yelshin, *Trans. Filtration Society* 1, 101 (2001).
49. G. Castro, and S.R. Nutt, *Mater. Sci. Eng., A* 535, 274 (2012).
50. T.R. Jonas, J.A. Cornie, and K.C. Russell, *Metall. Mater. Trans. A* 26, 1491 (1995).
51. N. Nicom, and H. Nomura, *Mater. Sci. Eng., A* 441, 97 (2006).
52. P. Yu, M. Qian, L. Li, and G.B. Schaffer, *Acta Mater.* 58, 3790 (2010).
53. M. Kida, M. Bahraini, J.M. Molina, L. Weber, and A. Mortensen, *Mater. Sci. Eng., A* 495, 197 (2008).
54. A. Léger, L. Weber, and A. Mortensen, *Acta Mater.* 91, 57 (2015).